

Remarks

Applicant and the undersigned would like to thank the Examiner for his efforts in the examination of this application. Reconsideration is respectfully requested.

I. Rejection of Claims 11 and 24 under 35 USC 112

The Examiner has rejected Claims 11 and 24 under 35 USC 112, second paragraph, as being indefinite.

This rejection is respectfully traversed. The term *thin function* does indeed have a standard meaning in the art, as attested to be the two Attachments A (from a NASA website; see paragraph 1) and B (Murthy et al., "An Analysis of 17 Years of *Voyager* Observations of the Diffuse Far-Ultraviolet Radiation Field," *Astrophys. J.* **522**, 904-14, 1999) and also as quoted from the book *Algorithms for Graphics and Image Processing* (T. Pavlidis, Computer Science Press, 1982): "The thin function returns the 'skeleton' of a bi-level image. The skeleton of an object in an image is a set of lines that reflect the shape of the object. The set of skeletal pixels can be considered to be the medial axis of the object."

Therefore, Claims 11 and 24 are believed free from indefiniteness.

II. Rejection of Claims 1, 2, 7, 8, 10, 12-15, 20, 21, 23, 25, 26, 30, 33, and 37 under 35 USC 103(a)

The Examiner has rejected Claims 1, 2, 7, 8, 10, 12-15, 20, 21, 23, 25, 26, 30, 33, and 37 under 35 USC 103(a) as being unpatentable over Williams et al. (US 6,394,999) in view of Knopp et al. (US 5,865,832).

Independent Claims 1, 13, 14, 26, and 33 have been amended to more particularly point out that which Applicants regard as their invention.

In particular, Claims 1, 13, and 14 have been amended to incorporate the element of allowable Claim 5, namely, that the first image map is filtered to reduce noise.

Claims 26 and 33 have been amended to incorporate the elements of allowable Claims 27-29, wherein the feature is recited as being one of a sclera blood vessel, a retinal blood vessel, and a retinal nerve.

Therefore, Claims 1, 13, 14, 26, and 33, as well as Claims 2, 7, 8, 10, 12, 15, 20, 21, 23, 25, 30, and 37 dependent therefrom, are believed patentable over the cited art.

III. Allowable Subject Matter

The Examiner has indicated Claims 3-6, 9, 16-19, 22, 27-29, 31, 32, 34-36, 38, and 39 to contain allowable subject matter, which Applicants acknowledge with appreciation.

Of this allowable group, Claims 5, 9, 18, 22, 27-29, and 34-36 have been canceled in order to incorporate their elements as discussed above into independent claims.

IV. Additional Claim Amendments

Claim 4 has been amended to correct dependency thereof to Claim 3.

Claim 6 has been amended to change dependency from now-canceled Claim 5 to Claim 1.

Claim 19 has been amended to change dependency from now-canceled Claim 18 to Claim 14.

Claim 37 has been amended to correct a typographical error, changing "charge-couple-device" to charge-coupled-device.

Conclusions

Applicants respectfully submit that the above amendments place this application in a condition for allowance, and passage to issue is respectfully solicited. The Applicants and the undersigned would like to again thank the Examiner for his efforts in the examination of this application and for reconsideration of the claims as amended in light of the arguments presented. If the further prosecution of the application can be facilitated through telephone interview between the Examiner and the undersigned, the Examiner is requested to telephone the undersigned at the Examiner's convenience.

Respectfully submitted,



Jacqueline E. Hartt, Ph.D.

Reg. No. 37,845

ALLEN, DYER, DOPPELT, MILBRATH & GILCHRIST, P.A.

255 South Orange Avenue, Suite 1401

P.O. Box 3791

Orlando, Florida 32802

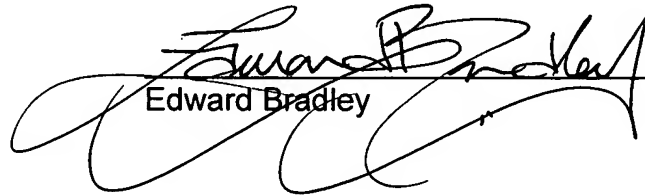
(407) 841-2330

Agent for Applicants



CERTIFICATE OF MAILING

I hereby certify that the foregoing is being deposited with the United States Postal Service as first class mail in an envelope addressed to the Commissioner for Patents, P.O. Box 1450, Alexandria, VA 22313-1450, this 23rd day of September, 2004.


Edward Bradley

[Categories](#) | [Alphabetical](#) | [Classes](#) | [All Contents](#) | [[<](#)] | [[>](#)]

Attachment A

THIN

SEP 27 2004

[Syntax](#) | [Return Value](#) | [Arguments](#) | [Keywords](#) | [Examples](#) | [Version History](#) | [See Also](#)

The THIN function returns the "skeleton" of a bi-level image. The skeleton of an object in an image is a set of lines that reflect the shape of the object. The set of skeletal pixels can be considered to be the medial axis of the object. For a much more extensive discussion of skeletons and thinning algorithms, see *Algorithms for Graphics and Image Processing*, Theo Pavlidis, Computer Science Press, 1982. The THIN function is adapted from Algorithm 9.1 (the classical thinning algorithm).

On input, the bi-level image is a rectangular array in which pixels that compose the object have a nonzero value. All other pixels are zero. The result is a byte type image in which skeletal pixels are set to 2 and all other pixels are zero.

Syntax

`Result = THIN(Image [, /NEIGHBOR_COUNT] [, /PRUNE])`

Return Value

Returns the thinned, two-dimensional byte array.

Arguments

Image

The two-dimensional image (array) to be thinned.

Keywords

NEIGHBOR_COUNT

Set this keyword to select an alternate form of output. In this form, output pixel values count the number of neighbors an individual skeletal pixel has (including itself). For example, a pixel that is part of a line will have the value 3 (two neighbors and itself). Terminal pixels will have the value 2, while isolated pixels have the value 1.

PRUNE

If the PRUNE keyword is set, pixels with single neighbors are removed iteratively until only pixels with 2 or more neighbors exist. This effectively removes (or "prunes") skeleton branches, leaving only closed paths.

Examples

The following commands display the "thinned" edges of a Sobel filtered image:

```
; Open a file for reading:
OPENR, 1, FILEPATH('people.dat', SUBDIR = ['examples', 'data'])

; Create a byte array in which to store the image:
A = BYTARR(192, 192)

; Read first 192 by 192 image:
READU, 1, A

; Close the file:
CLOSE, 1

; Display the image:
TV, A, 0

; Apply the Sobel filter, threshold the image at value 75, and
```

```
; display the thinned edges:  
TVSCL, THIN(SOBEL(A) GT 75), 1
```

Version History

Introduced: Pre 4.0

See Also

[ROBERTS, SOBEL](#)

[Categories](#) | [Alphabetical](#) | [Classes](#) | [All Contents](#) | [[<](#)] | [[>](#)]

AN ANALYSIS OF 17 YEARS OF *VOYAGER* OBSERVATIONS OF THE DIFFUSE FAR-ULTRAVIOLET RADIATION FIELD

JAYANT MURTHY, DOYLE HALL, MATTHEW EARL,¹ AND R. C. HENRY
 Department of Physics and Astronomy, Johns Hopkins University, Baltimore, MD 21218-2686

AND

J. B. HOLBERG
 Lunar and Planetary Laboratory, University of Arizona, Tucson, AZ 85721
 Received 1997 April 21; accepted 1999 February 10

ABSTRACT

We have systematically reduced 17 years of data from the *Voyager* ultraviolet spectrometer (UVS) archives, from which we have obtained 431 spectra that place useful limits on the diffuse far-ultraviolet radiation field between 912 and 1100 Å. We observe a large range in brightnesses ranging from upper limits of 30 photons cm⁻² s⁻¹ sr⁻¹ Å⁻¹. The diffuse background is correlated with the integrated *TD-1* flux near the line of sight but shows no correlation with *N*(H I). We place a 1 σ upper limit of 30 photons cm⁻² s⁻¹ sr⁻¹ Å⁻¹ on the level of an isotropic extragalactic continuum.

We have modeled and characterized the observed heliospheric H I and He I emission lines in the outer solar system as a function of heliospheric distance, apex angle from the direction of the inflowing interstellar wind, and time as specified by subspacecraft solar intensity. This modeling adequately reproduces observed intensities over a range of heliospheric distances of 15–50 AU, for an unrestricted range of look directions, and for a 12 year period (covering 1 solar cycle).

Subject headings: diffuse radiation — ultraviolet: ISM

1. INTRODUCTION

There are many different processes contributing to the diffuse celestial ultraviolet radiation field: heliospheric emission lines from within the solar system; the scattering of starlight from interstellar dust, emission from hot halo gas, and molecular hydrogen fluorescence in the interstellar medium (ISM); and extragalactic sources such as emission from an intergalactic medium, the integrated light of galaxies or quasars, or perhaps even emission from the decay of massive neutrinos (Sciama 1990). Unfortunately, there are very few reliable observations of the ultraviolet background (see Murthy & Henry 1995; reviewed by Bowyer 1991 and Henry 1991), because of both the faintness of the signal and the need for space-based instrumentation. In this context, there has been a surprising neglect of the *Voyager 1* and 2 ultraviolet spectrometer (UVS) archives. Comprising more than 17 years of data from the long stretches when the two spacecraft were between their highly successful planetary encounters, these archives contain observations of a wide variety of astrophysical targets in the spectral region between 550 and 1700 Å. In the best cases, limits of about 100 photons cm⁻² s⁻¹ sr⁻¹ Å⁻¹ (Holberg 1986; Murthy, Henry, & Holberg 1991) have been set on the diffuse radiation field—sufficient to significant constrain the various components of the UV background.

There are a total of 8376 observations in the *Voyager* archives,² and we have plotted the distribution of these in an Aitoff projection in Figure 1. Of these, 1766 were classified as “sky” by the original investigator, implying a

planned observation of the sky background; however, many more observations were of point sources that turned out to be too faint to detect with the *Voyager* UVS, resulting in a fine observation of the diffuse radiation field. We have completed the first phase of a project to systematically reduce and analyze all of the diffuse observations in the *Voyager* archives. After rejection of planetary and instrumental observations and after a careful cross-check with the SIMBAD database to reject point-source contaminants, we were left with a total of 431 spectra of various locations in the sky (Fig. 1, *diamonds*), some of which were multiple observations of the same position. In this work, we will concentrate on presenting the techniques used and will discuss the implications of these data for the UV background. The actual spectra and detailed results for each of the observations are available from the authors of this work and will be archived at the Astronomical Data Center.

In this paper we describe the scope of the *Voyager* data set and our techniques for the selection, verification, and analysis of the background observations presented here. In § 4 we present a comprehensive analysis of the H I Ly α and He I λ 584 heliospheric emission lines observed by *Voyagers 1* and 2 in the outer solar system. Also in § 4, we present a global summary of the distribution and intensity of the cosmic radiation field observed by the *Voyager* spacecraft in the 912–1100 Å band.

2. OBSERVATIONS

2.1. The *Voyager* Spacecraft and Mission

The two *Voyager* ultraviolet spectrometers are identical Wadsworth-mounted objective grating spectrometers, which cover the spectral range between 500 and 1700 Å over a field of view of 0°1 × 0°87. The spectral resolution of the instruments is 38 Å for aperture-filling diffuse sources and 18 Å for point sources. In addition to the primary aperture (the airglow port), there is a small off-axis port (the

¹ Current address: Department of Physics and Astronomy, Boston University, Boston, MA 02215.

² While *Voyager* observations continue to the present date, we have cut off this analysis in mid-1994. We will process the remainder of the observations in the near future.

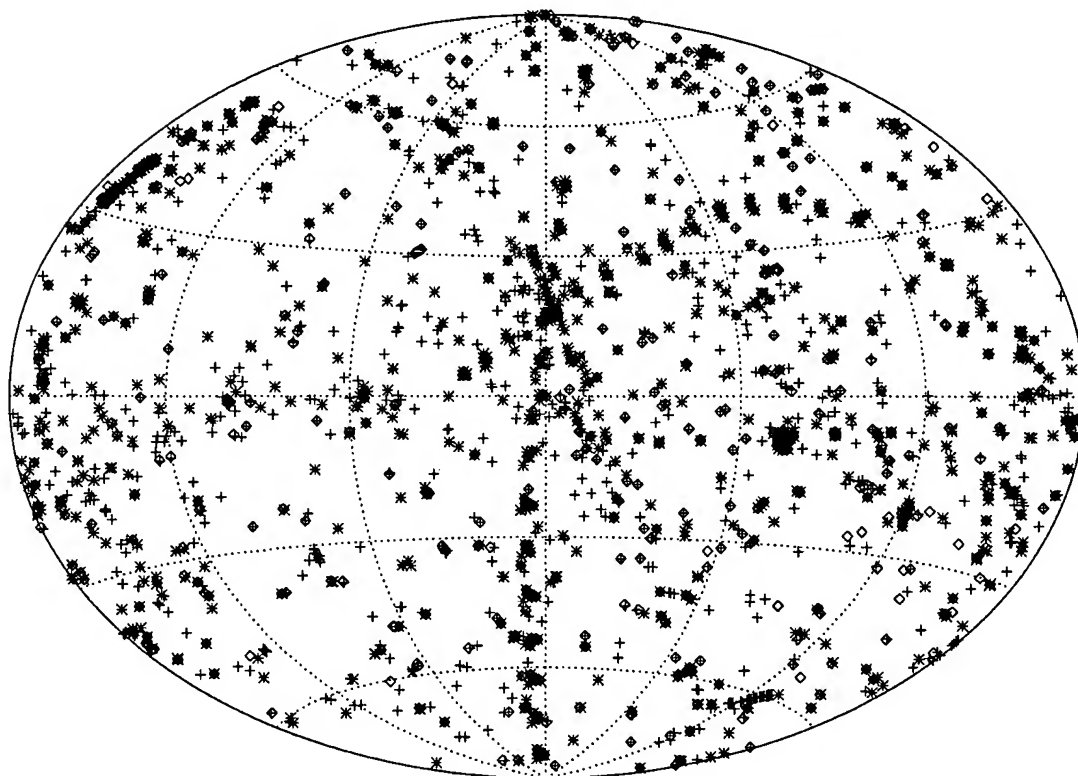


FIG. 1.—All 8376 *Voyager* observations in the mission log are plotted as plus signs on an Aitoff projection of the sky. The Galactic center is at the center of the plot, north is at the top, and longitude increases to the left. The 431 diamonds show the locations of those observations we have identified as being of the diffuse radiation field. Note that there are a handful of diamonds without an associated plus sign. Some of these are due to transcription errors while the values were entered into the mission log; the rest are due to small differences in the way the direction of observation is defined.

occultation port) designed to allow direct viewing of the Sun. For occasional unfortunate geometries, it is possible that a bright source seen through the occultation port will contaminate a faint source in the airglow port. The detectors are bare dual microchannel plates read out onto a linear self-scanned array of aluminium anodes, 126 of which are active for a bin size of 9.26 \AA . The UVS is most sensitive at wavelengths below 1200 \AA , with a rapidly declining response at longer wavelengths. At wavelengths longward of 1280 \AA , the microchannel plate detectors are covered by a MgF_2 window with a semitransparent CsI coating. This window, designed to increase the response of the bare glass microchannel plate at long wavelengths, introduces a spectral artifact centered on channel 81 and a discontinuity between the long- and short-wavelength halves of the detector.

The two spacecraft were launched within a month of each other—*Voyager 2* in 1977 August and *Voyager 1* in 1977 September—on their mission to explore the giant planets. *Voyager 1* encountered Jupiter and Saturn in 1979 and 1980, respectively, while *Voyager 2* encountered all four Jovian planets, culminating in the Neptune encounter in 1989. Both spacecraft are now approximately 50 AU from the Sun, and receding by about 3 AU per year. Observations with the UVS continue to the present date and should do so until about the year 2000, when there will be insufficient power from the spacecraft radioisotope thermoelectric generator (RTG) to operate the instruments. A full description of the UVS instruments and further infor-

mation about the *Voyager* mission is given by Holberg & Watkins (1992).

2.2. Data Processing

A typical *Voyager* sky observation consists of a series of individual spectra (often termed accumulations) with an onboard integration time of (most commonly) 3.84 or 576 s, although intermediate integration times were also used at different times in the mission. The total exposure time for a single observation can range from a few hundred to several million seconds, with exposure times greater than 10^4 s being the most useful for observations of the diffuse radiation field. The data are transmitted to the Earth at regular intervals, where they are acquired by the Deep Space Network antennas in Spain, California, and Australia, are sent to the Jet Propulsion Laboratory in California, and finally are sent to the Lunar and Planetary Laboratory (LPL) in Arizona, where they are currently archived. The entire *Voyager* archives now occupy about 10 gigabytes and may be searched and retrieved over the Internet. As we desired to process the entire database, we acquired the complete (to 1994) data set on five 8 mm tapes.

A number of IRAF routines exist at LPL to analyze the *Voyager* UVS data interactively, which we recommend to the general user. However, this software is not suitable for the automatic extraction of thousands of spectra, and we have developed our own software optimized for the analysis of diffuse sources (the analysis of point-source observations may involve informed decisions by the analyst and would

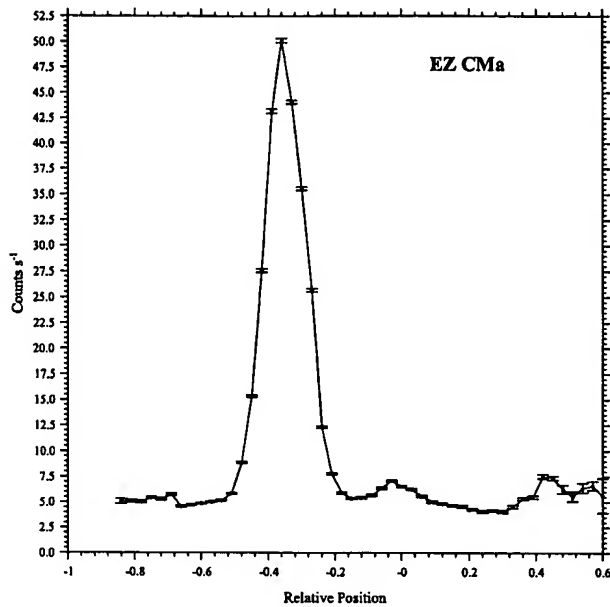


FIG. 2.—The total signal observed from the star EZ CMa, plotted as function of the limit-cycle motion of the spacecraft on the sky. Because the response function changes across the aperture, any point source will show the same characteristic profile. We have used this behavior as a sensitive test (to an equivalent V magnitude of 16 for a B star) for point sources in the field of view.

complicate our software considerably). We have used the Interactive Data Language (RSI, Boulder) for this task, and our programs are available upon request. We emphasize that, as with any major data set, analyzing *Voyager* data from scratch is not a trivial task and should not be done without adequate preparation.

The archival *Voyager* data are stored as a time-ordered series of records on several 8 mm tapes. At the beginning of each record is a header, containing such information as the date for each individual accumulation, and the mode of

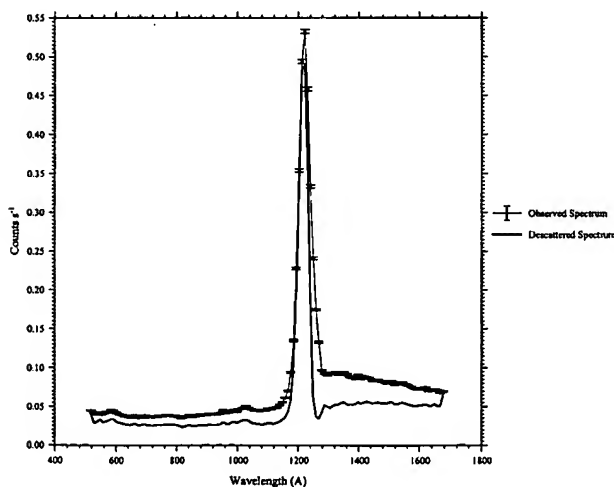


FIG. 3.—An arbitrary *Voyager* 2 spectrum (in the direction of the Seyfert galaxy NGC 4151), plotted as a thin line with 1σ error bars. The strongest feature in this, as in almost every UVS spectrum, is heliospheric Ly α at 1216 Å. The scattering wings of the line extend throughout the spectrum but can be removed by application of a “descattering” operator. The descattered spectrum is shown as the dark line. We have chosen this particular spectrum arbitrarily and purely for illustrative purposes.

operation, followed by the actual data. The mission log, which is maintained as a regularly updated text file at LPL, contains the start and stop dates of each observation (as well as other observational parameters) and we used those dates to extract all the data for a single observation into a file on a hard disk. A few corrupted accumulations (largely due to transmission errors over the long interplanetary distances traversed) were discarded and the remainder added together to form a single spectrum of the region observed.

Because most of the *Voyager* observations were nominally of point sources, we must ensure that the signal observed is truly diffuse. Such a test is provided by the limit-cycle motion of the spacecraft. As the slit moves across a point source, the observed signal will vary as a function of w , the off-axis angle. If the χ^2 fit of a flat line to the data was significantly greater than unity, we rejected that observation as being unambiguously due to a point source (or sources), as is the case (for example) with the observation of EZ CMa that is plotted in Figure 2. A further refinement was to actually fit a sample response function to the data and thereby set limits on the maximum contribution of a point source to the data. It should be noted that this test is optimized to the detection of faint point sources rather than extended sources with spatial structure (e.g., supernova remnants).

The only potential contributors of direct starlight to UVS observations are luminous O and B stars and hot sub-luminous stars. In the case of the former it can be shown that at signal levels of several hundred photons $\text{cm}^{-2} \text{s}^{-1} \text{Å}^{-1}$, the apparent magnitude of a single unreddened B star of equivalent brightness must be greater than $V = 11$ (Holberg 1990). However, a B star of such low apparent magnitude must be at a distance greater than 10 kpc, and the signal in the 900–1200 Å band would be considerably attenuated by interstellar absorption. Hot sub-luminous stars are readily detected by the UVS and can, in principle, contribute to a diffuse signal. However, the space densities of these objects are very low, and the above test for point sources can readily identify the presence of such stars to a limiting magnitude (V) of 16. We have searched through both the *TD-1* and *SIMBAD* catalogs for the presence of hot stars and have rejected those observations with possible contamination.

The last step before extraction of the heliospheric and cosmic signals was to combine those *Voyager* observations that were split into several parts in the mission log, for various spacecraft maintenance-related reasons. As our procedure was based on entries in the log files, each part of such an observation was reduced separately and created independent files. We went through the entire data set and, based on observation names and positions, combined these individual spectra. We then eliminated all observations that were not astronomical in nature (planetary and calibration observations) and those with possible point-source contamination. This left us with a total of 431 observations that we believe are true observations of the diffuse radiation field and are plotted as diamonds in Figure 1.

3. DATA ANALYSIS

We have plotted the spectrum of an arbitrary region in space (labeled as an observation of NGC 4151 in the UVS archives) in Figure 3. The single most prominent feature in the observed spectrum is almost always the heliospheric Ly α line at 1216 Å, which is so intense that its scattering

wings extend over virtually the entire spectrum. Fortunately, the scattering function was measured accurately on the ground prior to flight, and a descattering operator, consisting of an individual 126×126 element matrix for each spacecraft, was defined. This matrix was applied to every spectrum after the removal of dark counts, and its effects may be seen from the difference between the two spectra plotted in Figure 3. Although the scattering function did change somewhat during the mission, the effects of these changes are greatest on the long-wavelength side of $\text{Ly}\alpha$ and are less important in the spectral regime between 912 Å and the $\text{Ly}\alpha$ line, where our greatest interest lies.

There are three independent constituents of the typical UVS spectrum: dark noise from the spacecraft's radioisotope thermoelectric generator (RTG), emission lines from the interplanetary medium, and a cosmic signal (which we define to be all radiation originating beyond the solar system). The RTG spectrum for each spacecraft was measured at regular intervals by pointing the UVS at a calibration plate shadowed by the spacecraft body, and we have plotted scaled RTG spectra from several years for each spacecraft in Figure 4. The spectra are virtually identical except in the vicinity of $\text{Ly}\alpha$, where heliospheric emission is reflected by the calibration plate into the UVS. The stability of the RTG emission—in shape, not in scale—allowed us to choose a single measurement from late in the mission, when the heliospheric emission was at a minimum, for each spacecraft. We then scaled the RTG spectrum to each observation using a least-squares fit in the channels between the He line at 584 Å and the Lyman limit at 912 Å. This implicitly assumes that the observed continuum in this region is instrumental in origin with no astronomical contribution; a valid assumption for all but a handful of nearby stars. The data reduction procedures outlined here are discussed in more detail in Holberg (1986).

Present in every spectrum are the heliospheric lines of helium and hydrogen—He at 584 Å, $\text{Ly}\alpha$ at 1216 Å, $\text{Ly}\beta$ at 1026 Å, and, early in the mission, $\text{Ly}\gamma$ at 972 Å. The helium line is easily isolated and its intensity measured because of the lack of any other contributors in its vicinity. However, the Lyman lines are located in the midst of the astrophysical

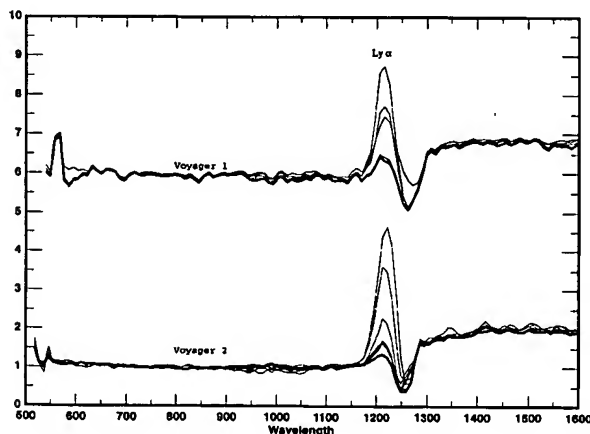


FIG. 4.—RTG spectra for each spacecraft do not change much with time, as is shown in this composite plot of a number of observations of a calibration plate on each spacecraft from different years. Except near the $\text{Ly}\alpha$ line, where heliospheric emission is backscattered from the plate into the UVS, there is little difference between the lines. In our data analysis we have used an RTG spectrum from 1989 for *Voyager 1* and one from 1993 for *Voyager 2*, both of which are plotted as thick lines in the figure.

signal and must be modeled in conjunction with it. The characteristic shape for a diffuse emission-line source in the UVS spectrum is a convolution of two triangles with respective widths of 3.54 and 2.3 bins (where each bin is 9.26 Å), and we used this profile (which is almost indistinguishable from a Gaussian of FWHM 38 Å) as a model for both the $\text{Ly}\beta$ and $\text{Ly}\gamma$ lines. The intense $\text{Ly}\alpha$ was not fitted well by such a model, and we used instead an actual spectrum in which there was no astrophysical continuum, as a template for this line. As mentioned above, the shape of the $\text{Ly}\alpha$ line did change over the lifetime of the mission, especially after stressing events such as a direct observation of the Sun or passage through the Jovian magnetosphere, and we were forced to use different templates at different periods in the spacecraft lifetime (Table 1). At first we truncated the spectrum immediately on either side of the line but found a residual with features repeatable over different spectra and at a level correlated with the strength of the $\text{Ly}\alpha$ line. We identified this residual as being due to imperfectly removed scattered $\text{Ly}\alpha$ and incorporated it into our template.

Much less is known, a priori, about the diffuse cosmic radiation field and its sources in any particular region of the sky, and we are currently in the process of developing a comprehensive model to predict the cosmic background from any direction in the sky. In this work, we concentrate on presenting the values as observed, and we have used the model developed by Murthy & Henry (1995) to predict the spectral shape of the component due to dust-scattered starlight for each observation. In general, the spectrum is similar to that of an early B star but does differ somewhat in different locations depending on the characteristics of the stars contributing to the scattering in the line of sight.

Finally, we simultaneously fitted the heliospheric Lyman lines on the continuum representing the cosmic background to the data using a minimum χ^2 procedure, with the greatest weight placed on the fit between 900 and 1150 Å, where the sensitivity of the UVS to a cosmic signal is greatest. The $\text{Ly}\alpha$ line is so much stronger than any other signal that its fit

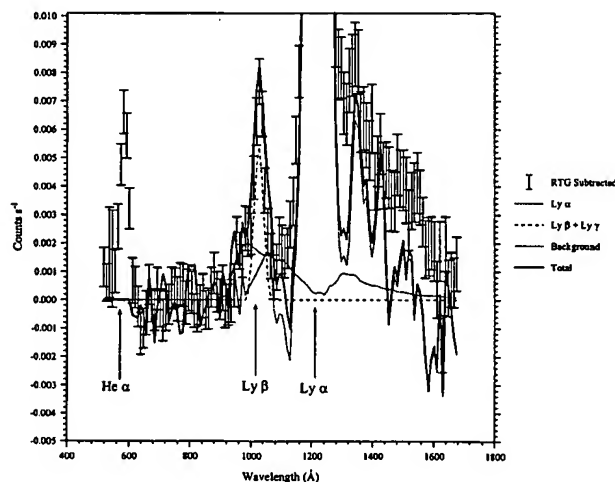


FIG. 5.—Different components of our fit to NGC 4151. The RTG spectrum has been scaled and subtracted, and the signal between He α and 900 Å is zero, as it should be. The fit at wavelengths longward of $\text{Ly}\alpha$ is not very good; it is better in many of the observations. However, we do not consider that spectral region because of the low sensitivity of the UVS there (as may be seen from the fall-off in the model of the cosmic background). We repeat that we have chosen this spectrum for illustrative purposes only.

TABLE 1
Voyager Templates

Dates	Target ^a	Observation Date	<i>l</i> (deg)	<i>b</i> (deg)	Exposure Time ^b	σ^b
<i>Voyager 1 Lyα Templates</i>						
77/287–79/104	SKY	78/048	115.5	–22.7	96,180	383
79/110–80/227	RS CVn	80/122	96.9	80.3	329,805	139
80/227–83/006	NGP	81/306	200.2	89.6	658,328	110
83/021–90/176	SKY	88/343	92.9	48.4	225,705	168
90/191–92/056	Spica 3	91/329	324.3	53.9	231,600	142
92/059–93/078	V1–V2	92/086	92.4	67.3	461,520	161
93/099–94/057	Nova Cyg	93/102	89.0	7.5	326,795	177
<i>Voyager 2 Lyα Templates</i>						
78/037–78/080	Alp UMi	78/053	97.7	–60.2	214,500	96
78/086–78/207	SKY	78/124	91.1	61.4	381,087	63
78/208–79/106	SKY	78/279	35.1	–9.8	199,360	82
79/240–79/331	SC34AE13	79/296	97.7	–60.2	41,827	87
79/333–80/051	HZ 43	80/039	54.2	84.1	119,424	88
80/052–80/351	HZ 44	80/101	87.7	78.7	160,704	116
80/353–82/018	NGP	81/069	304.2	90.0	114,048	110
82/018–85/226	PG 1211 + 143	88/196	267.6	74.3	61,218	116
85/231–89/124	NGC 5548	88/327	32.0	70.5	574,589	62
89/128–92/031	PKS 2155–304	89/285	17.7	–52.2	268,556	59
92/034–92/092	RE 0134–160	92/031	167.3	–75.2	94,542	102
92/099–92/230	V2 anti V1	92/092	272.5	–67.4	166,503	57
92/233–93/123	HD 129333	92/230	105.5	49.1	116,086	72
93/142–93/351	NGP	93/260	33	90	71,899	138
93/351–94/059	BKGND 4	94/014	78.2	0.6	268,088	66

NOTE—Dates are given in the form year/day, e.g., 83/021 = 1983 Jan 21.

^a As defined in the mission log.

^b Uncertainty in background in units of photons cm^{–2} s^{–1} sr^{–1} Å^{–1}.

was essentially a normalization of the template spectrum to the peak of the observed signal. The different components of our fit are illustrated in Figure 5, where we have plotted the *Voyager 2* spectrum in the direction of NGC 4151.

TABLE 2
Ly β /Ly α RATIO

Spacecraft	Dates	Ratio
1	77/287–94/057	0.044 ± 0.027
2	78/037–81/155	0.078 ± 0.0065
2	81/155–89/147	0.092 ± 0.014
2	89/281–94/059	0.0576 ± 0.019

In our first run through the data, we allowed the Ly β /Ly α ratio to vary freely. However, because the Lyman lines are optically thick, we would expect that the Ly β /Ly α ratio would remain constant, although, of course, the strength would not. We tested this hypothesis by selecting those observations of greater than 50,000 s in length in which there was no evidence of any astrophysical signal, i.e., where the observed signal was entirely heliospheric. The Ly α and Ly β strengths in the *Voyager 2* spectra are plotted as a function of time in Figure 6a and the ratio is plotted in Figure 6b. While there is a strong correlation between the two Lyman lines (Fig. 6a), the ratio appears to show two breaks, one in mid-1981 and the second at the beginning of 1989 (Table 2). It is known (Hall 1992) that the Ly α

TABLE 3
OBSERVATIONS OF THE NORTH GALACTIC POLE

Spacecraft	Observation Date	Exposure Time	<i>l</i>	<i>b</i>	Background ^a	Uncertainty ^b
		(s)	(deg)	(deg)		
2	79/278	7073	304.2	90.0	0	328
2	81/069	114048	304.2	90.0	0	110
2	81/071	85824	304.2	90.0	35	113
2	81/079	24771	304.3	90.0	426	201
2	81/080	153216	304.2	90.0	61	68
2	81/082	130692	304.2	90.0	0	114
1	81/306	658328	200.2	89.6	0	110
1	82/068	221016	128.5	89.4	0	213
2	93/260	71899	33.0	90.0	18	138

^a Flux at a wavelength of 1100 Å in units of photons cm^{–2} s^{–1} sr^{–1} Å^{–1}.

^b 1 σ uncertainty in units of photons cm^{–2} s^{–1} sr^{–1} Å^{–1}.

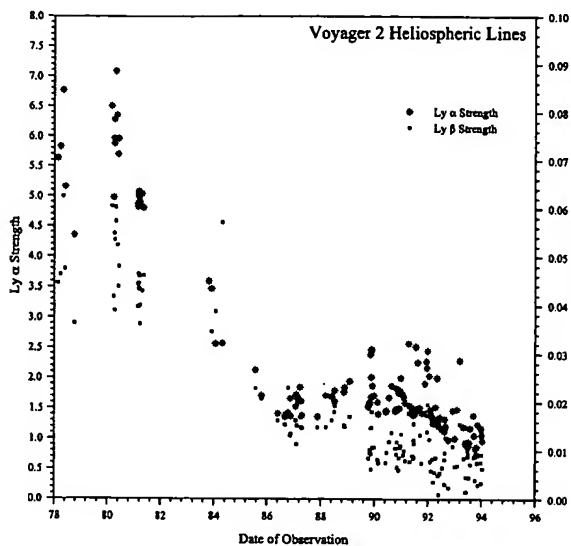


FIG. 6a

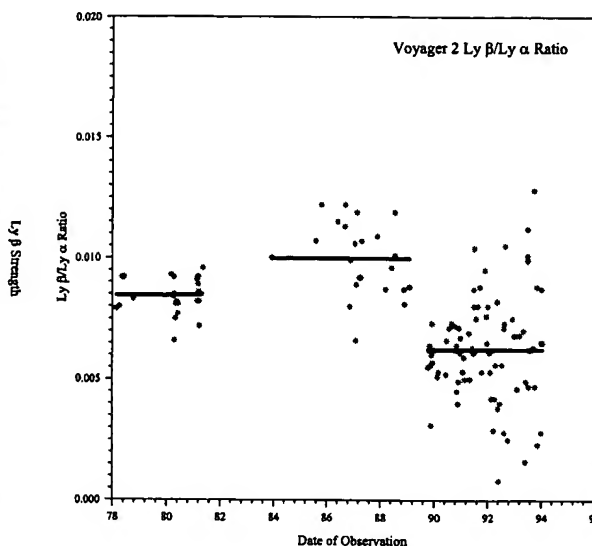


FIG. 6b

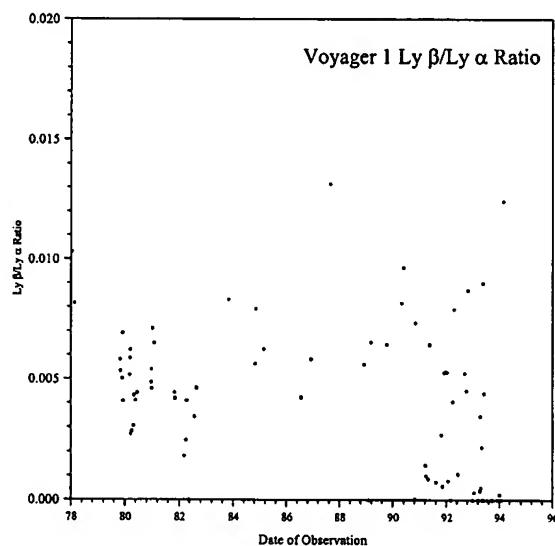


FIG. 6c

FIG. 6.—(a) $\text{Ly}\alpha$ and $\text{Ly}\beta$ line strengths for *Voyager 2*, shown as a function of observation date. (b) Plots of $\text{Ly}\beta/\text{Ly}\alpha$ ratios. Note that late in the mission, the $\text{Ly}\beta$ line is hard to distinguish from the background level, and there is a large scatter in determining its level. The gaps in the observed data points are due to planetary encounters, and it appears that the $\text{Ly}\beta/\text{Ly}\alpha$ ratio is different after each gap. Although both the $\text{Ly}\alpha$ and $\text{Ly}\beta$ lines are optically thick and their ratio should not change, we have empirically assumed three different ratios (solid lines in [b]) and used those ratios in our analysis. No such changes were seen in the *Voyager 1* ratio (c). We note that fixing the $\text{Ly}\beta/\text{Ly}\alpha$ ratio (rather than letting it vary freely) had less than a 5% effect on the derived continuum value.

response of the *Voyager 1* UVS was degraded during its passage through the Jovian magnetosphere, and it is likely that the varying $\text{Ly}\beta/\text{Ly}\alpha$ ratio empirically observed in the *Voyager 2* data (Fig. 6b) is due to different rates of degradation in the spectral regions covered by the two lines. We found no similar changes in the $\text{Ly}\beta/\text{Ly}\alpha$ ratio in the *Voyager 1* data (Fig. 6c), and the ratio used throughout the observation period is tabulated in Table 2. It should be noted that the overall calibration of both instruments has remained constant over the 17 years covered by our observations (Holberg et al. 1991). In actuality, because the fitting procedure determines the continuum intensities through a fit of the entire spectrum between 912 and 1100 Å, fitting the $\text{Ly}\beta/\text{Ly}\alpha$ ratio had virtually no impact ($< 5\%$) on the background values derived in this work.

In order to check the consistency of our procedure, we have selected a subsample of the observations for which there was at least one other observation within 1° . There were 188 such observations. For each of these groups of observations (i.e., those observations which were near each other) we calculated the mean value of the derived background values and the deviation of each observation from that mean. Only 11 (6%) of the observations fell more than 3σ away from the mean, 28 (15%) fell more than 2σ from the mean, and 61 (32%), fell beyond 1σ from the mean, entirely consistent with a normal distribution of errors. This is a very important result. Although many years separated some of these observations and different spacecraft with entirely different viewing geometries (through the solar system) were used to make the observations, there is no

effect on our derived background values. We note that this is a postreduction result (no attempt was made *a priori* to ensure consistency) and forces us to believe that our reduction procedure is, at least, self-consistent and that the error bars are reasonable.

4. RESULTS

4.1. Heliospheric Resonance Lines

In addition to diffuse background radiation emitted from very distant astronomical sources, the *Voyager* UVS instruments also detect photons resonantly scattered from atomic hydrogen and helium in interplanetary space and the very local interstellar medium (Holberg 1986; Broadfoot et al. 1981; see Thomas 1978 for a review of heliospheric resonance scattering). Both *Voyager* spacecraft are traveling into the upstream direction of the local interstellar flow. The strongest heliospheric resonance line, H I $\lambda 1216$, is easily observable in all UVS spectra, and two other lines, H I $\lambda 1025$ and He I $\lambda 584$, are measurable in the longer duration UVS observations. Heliospheric resonance line intensities depend sensitively on spacecraft heliocentric position r and look direction l . For $15 < r < 50$ AU, observed intensities looking into the antisolar direction (r) fall with increasing spacecraft heliocentric distance; also, intensities grow as the angle q between the look direction and the spacecraft direction vector increases. Here we present a semiempirical best-fit analysis of the distribution of UVS resonance line intensities as functions of r and θ that provides a simple approximate means of calculating upstream heliospheric H I $\lambda 1016$, H I $\lambda 1025$, and He I $\lambda 584$ intensities between 15 and 50 AU.

In look directions near stars or in regions of the sky with elevated diffuse background levels, H I $\lambda 1025$ is often severely blended with the background signal in the observed spectra. In the 912–1150 Å region of the spectrum, the mismatch between the data and best-fit model spectra can be a significant fraction of the best-fit H Ly β signal level, and the derived H Ly β intensities exhibit large, nonphysical variations from observation to observation, especially for $r > 15$ AU, where H Ly β signals are often overwhelmed by the diffuse background. In addition, because of the higher UVS noise levels on *Voyager 1*, the H I $\lambda 1025$ signal-to-noise ratios are often poor even for relatively long-duration exposures. Inside $r = 15$ AU, the *Voyager 2* spectra indicate that the ratio of H Ly α to H Ly β photon intensities is roughly 700 ± 200 (using the revised calibration of Holberg et al. 1991); *Voyager 1* spectra indicate a comparable ratio.

4.1.1. Heliospheric H I $\lambda 1216$ Variations

Earlier reductions of *Voyager* UVS heliospheric observations (Hall 1992; Hall et al. 1993) indicated that the H Ly α intensities beyond 15 AU from the Sun can be reproduced very well using the semiempirical formula

$$I(r, \theta, t) = I_0 J(\theta) [r_0/r(t)]^\kappa [F(t)/F_{\text{ref}}]^\gamma, \quad (1)$$

where I_0 is the intensity looking into the antisolar direction from an upstream position with heliocentric radial distance r_0 . The spacecraft heliocentric distance is $r(t)$, and the exponent κ describes the variation of the intensities with heliocentric distance. $F(t)$ is the variable subspacecraft solar H Ly α integrated line flux (as measured at 1 AU), and F_{ref} is a reference value for the solar H Ly α line flux, taken to be 3×10^{11} photons $\text{cm}^{-2} \text{s}^{-1}$ in this analysis. The exponent γ describes the approximate relationship between the solar

line-integrated flux and line-center flux (for instance, when the solar H Ly α line shape does not change significantly over the solar cycle, $\gamma = 1$). The function $J(\theta)$ describes the variation of intensity with θ , the angle between the sight line and the antisolar direction, and is defined such that $J(0) = 1$.

In a system with a uniform H atom density, when r is well within one H Ly α photon-scattering length scale (i.e., the optically thin, uniform density limit), the intensity is analytically derivable (see Hall 1992), and is found to fall as r^{-1} (so $\kappa = 1$ in this limit). In the optically thick, uniform density limit, κ is approximately 2 (Ivanov 1973). For isotropic resonance scattering, $J(\theta) = \theta/\sin \theta$ in the optically thin limit. For nonisotropic resonance scattering with a phase function of the form

$$\phi(a) = A + B \cos^2 a, \quad (2)$$

where α is the scattering angle, the optically thin function has the form

$$J(\theta) = \frac{A(\theta/\sin \theta) + (B/2)(\cos \theta + \theta/\sin \theta)}{A + B}. \quad (3)$$

The phase coefficients for H Ly α resonance scattering are $A = \frac{11}{12}$ and $B = \frac{3}{4}$ (Brandt & Chamberlain 1959). A least-squares analysis of the UVS H Ly α data acquired in the region $15 \text{ AU} < r < 35 \text{ AU}$, indicates that $\kappa = 0.95 \pm 0.04$ and $\gamma = 1.02 \pm 0.07$ for the combined *Voyager 1* and *Voyager 2* data. The function $J(\theta)$ can be approximated as

$$J(\theta) = \left(\frac{\theta}{\sin \theta} \right)^\mu, \quad (4)$$

with $\mu = 0.52$, a significantly different form from that expected for a uniform medium as given by equation (3). This difference is caused by the combined effects of multiply scattered H Ly α photons and the existence of an ionization cavity in the heliospheric H distribution carved by the solar wind and EUV radiation. The quality of this fit is shown in Figure 7 as a function of observation data (to illustrate the solar flux variation). The expansion using the best-fit parameters reproduces the H Ly α data to an rms accuracy of 22% and 15% for *Voyager 1* and *Voyager 2*, respectively. The solar H Ly α line-integrated flux as measured by the *SME* satellite and derived from the He I $\lambda 10830$ proxy (Tobiska 1991; Lean 1990), were used in this analysis, and the best-fit values for κ and μ are relatively insensitive to γ , yielding essentially the same results over the range $0.8 < \gamma < 1.2$. For $r_0 = 15$ AU, the best-fit values for I_0 are $(3.52 \pm 0.09) \times 10^7$ LU (1 LU = 1 photon $\text{cm}^{-2} \text{s}^{-1} \text{sr}^{-1}$) for *Voyager 1*, and $(3.67 \pm 0.07) \times 10^7$ LU for *Voyager 2*. These absolute intensities were derived using the H Ly α sensitivity calibration factors presented by Hall (1992), which account for the nonuniform sensitivity degradation that the *Voyager 1* UVS suffered during its traversal through the harsh radiation environment of Jupiter's magnetosphere. The difference between the best-fit values of I_0 for the two UVS instruments is most likely related to the uncertainty in their relative H Ly α sensitivities.

It is pertinent to note that the semiempirical expansion presented here applies only to *Voyager* data acquired between 15 and 50 AU from the Sun. Data acquired closer to the Sun by *Voyager* and other spacecraft must be modeled using a considerably more complicated calculation (see Pryor et al. 1992 for an example), although the best-fit

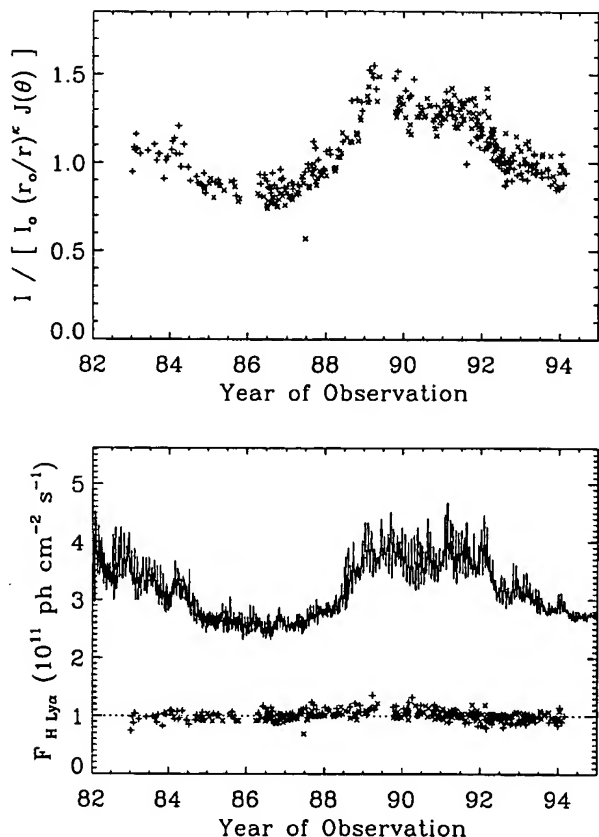


FIG. 7.—Variation of heliospheric H Ly α intensities measured between heliocentric distances of 15 and 50 AU as a function of observation date. The upper panel shows the observed intensities, corrected for variations with heliocentric radial distance r and antisolar angle θ . *Voyager 1* observations are shown as plus signs and *Voyager 2* observations as crosses. The lower panel shows the variation of the solar H Ly α line-integrated flux (solid line), and clearly indicates that the *Voyager* UVS data track the solar variations closely. Also plotted in the lower panel are the ratios of observed H Ly α intensities to the values calculated from the best-fit semiempirical expansion that reproduces the *Voyager 1* and 2 data to an rms accuracy of 22% and 15%, respectively.

form of $J(\theta)$ given by equation (3), with μ approximately equal to 0.5, appears to extend inward almost to 5 AU. In addition, the expansion presented here does not include the small excess emission detected by both *Voyager* spacecraft toward the exact direction of the upstream interstellar wind (Quemerais et al. 1995), an excess that may be of either heliospheric or Galactic origin. However, this excess emission is relatively faint (less than about 1.2×10^6 LU) and occupies a small section of the sky.

4.1.2. Heliospheric He I $\lambda 584$ Variations

An analysis of heliospheric He I $\lambda 584$ intensities is complicated by the lack of detailed knowledge of solar He I $\lambda 584$ variations during the observation period. Here, we use the solar H Ly α line flux variations as a proxy for the solar He I $\lambda 584$ variation. Using an expansion of the form in equation (1), we find that the *Voyager 2* He I $\lambda 584$ intensities between 15 and 50 AU are reproduced to an rms accuracy of 35% if $\gamma = 1.4 \pm 0.2$, $\kappa = 1$, and $J(\theta)$ is given by equation (3) with phase coefficients $A = B = 0.75$, appropriate for He I $\lambda 584$ resonance scattering. Thus, the analysis indicates the line-center He I $\lambda 584$ solar flux varies roughly as $F^{1.4}$, where F is

the solar H Ly α line-integrated flux. The fact that the data can be reproduced using the uniform density, optically thin form of equation (1) is not surprising because one optical depth for heliospheric He I $\lambda 584$ resonance scattering is known to correspond to a length scale of more than 200 AU, and models of the heliospheric He distribution indicate that the upstream He atom density should be essentially constant for $r > 5$ AU. For $r_0 = 15$ AU, we derive that $I_0 = (2.9 \pm 0.5) \times 10^4$ LU for He I $\lambda 584$.

4.2. Cosmic Radiation Field

The first attempts to measure the diffuse radiation field in the far-ultraviolet were made using Geiger counters with a 13° field of view aboard the *Venera* spacecraft (Belyaev et al. 1971) with reported intensities of between 1.7×10^3 and 36×10^3 photons $\text{cm}^{-2} \text{s}^{-1} \text{sr}^{-1} \text{\AA}^{-1}$. However, later observations (Henry 1973; Bixler, Bowyer, & Grewing 1984 and references therein) could not confirm the positive detections, instead placing upper limits of the order of 10^4 photons $\text{cm}^{-2} \text{s}^{-1} \text{sr}^{-1} \text{\AA}^{-1}$ on the diffuse radiation. The best observations to date have been obtained using the *Voyager* UVS. Sandel, Shemansky, & Broadfoot (1979) reported intensities of 2000–5000 photons $\text{cm}^{-2} \text{s}^{-1} \text{sr}^{-1} \text{\AA}^{-1}$ near Orion, and Holberg (1986, 1990) found only upper limits of 300 photons $\text{cm}^{-2} \text{s}^{-1} \text{sr}^{-1} \text{\AA}^{-1}$ or less everywhere except for two extended regions of about 2000 photons $\text{cm}^{-2} \text{s}^{-1} \text{sr}^{-1} \text{\AA}^{-1}$ in intensity, one near Ophiuchus and the other near Orion. The positive detections are all characteristic of stellar spectra and therefore represent either unresolved stars or scattered starlight.

To this small sample of data points, we have added 431 observations of 302 independent locations in the sky. We have taken pains to reject any observations which may have been contaminated by point sources. We examined each *Voyager* field using both the SIMBAD and *TD-1* databases for the presence of contaminating sources, rejecting those observations with a high signal for which a plausible source existed. Although this procedure may result in our rejecting

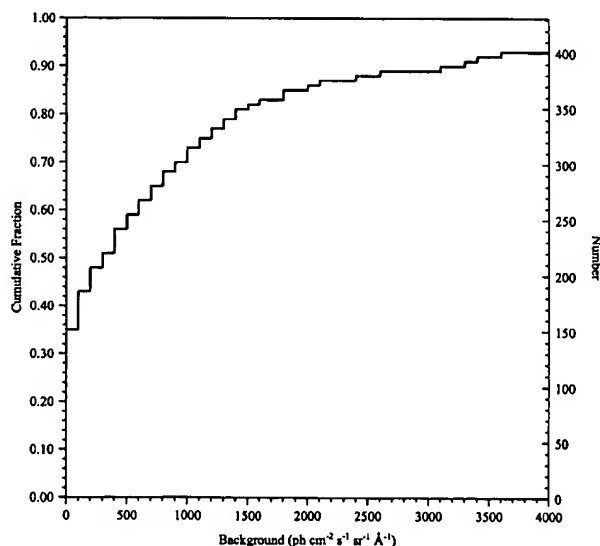


FIG. 8.—Distribution of our observed backgrounds, plotted as a histogram, in the 196 observations we consider to be the best estimators of the diffuse radiation field. There is a wide range in observed brightness, with the darkest being upper limits of less than 30 photons $\text{cm}^{-2} \text{s}^{-1} \text{sr}^{-1} \text{\AA}^{-1}$ and the brightest being levels of 30,000 photons $\text{cm}^{-2} \text{s}^{-1} \text{sr}^{-1} \text{\AA}^{-1}$.

a true background observation, we are confident that the remaining observations are unimpeachable.

The cumulative distribution of the derived backgrounds in these observations is shown in Figure 8. While almost 40% have intensities of under $100 \text{ photons cm}^{-2} \text{ s}^{-1} \text{ sr}^{-1} \text{ \AA}^{-1}$, there are a surprising number ($\sim 20\%$) with intensities over $2000 \text{ photons cm}^{-2} \text{ s}^{-1} \text{ sr}^{-1} \text{ \AA}^{-1}$, a bright signal indeed by the standards of studies of the diffuse radiation field. It has often been assumed that the diffuse background is directly correlated with the Galactic latitude or with the distribution of $N(\text{H I})$. In fact, there is no such simple relationship: the intensity of the diffuse background depends heavily on *local* causes, such as the presence of a nearby bright UV star and its location relative to the dust in the line of sight. This is illustrated by the data in Figure 9, where we have plotted the observed brightness as a function of the integrated brightness of all the *TD-1* sources (at 1565

\AA) within 10° of the observation. Despite the scatter in the plot, perhaps due to different dust distributions, it is clear that there is a strong correlation between the *TD-1* stars, which presumably trace the local radiation field, and the observed scattering from that direction. A similar plot with *TD-1* stars within 1° of the observed position shows no correlation, indicating that instrumental scattering does not affect our results. By contrast, there is no correlation with the H I column density (Fig. 9b) and only a mild correlation with the Galactic latitude (Fig. 9c), probably indirectly due to the correlation of UV-bright sources with Galactic latitude.

The dark areas observed in our sample are truly dark with (1σ) upper limits as low as $30 \text{ photons cm}^{-2} \text{ s}^{-1} \text{ sr}^{-1} \text{ \AA}^{-1}$. Many of these areas are at the highest Galactic latitudes, where one would expect the flux to be dominated by the extragalactic radiation field, if any, and their values are

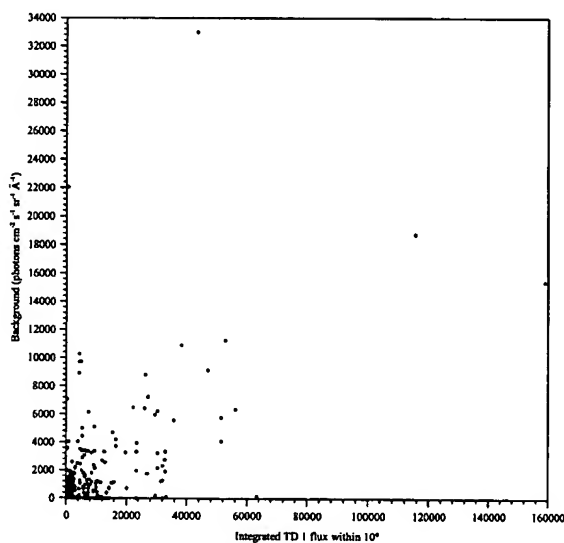


FIG. 9a

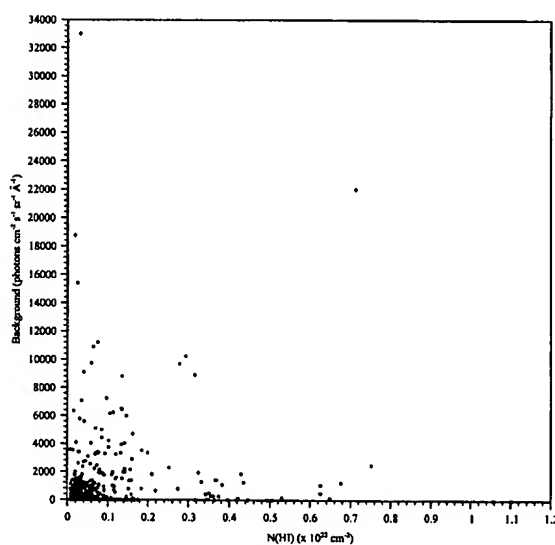


FIG. 9b

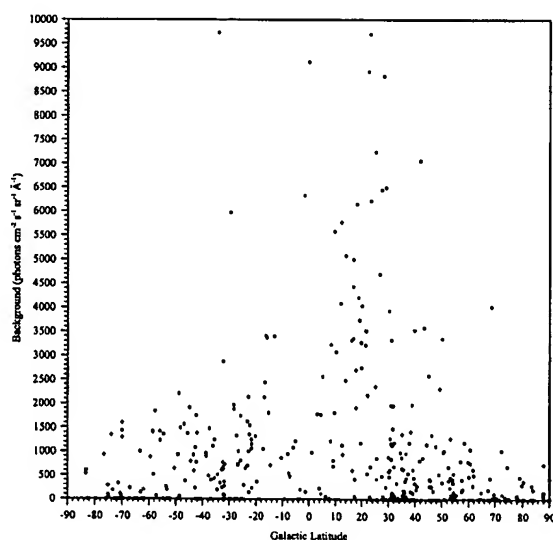


FIG. 9c

FIG. 9.—Plotted in (a) is the observed level of the diffuse radiation field as a function of the integrated flux from all the *TD-1* sources within 10° of the observation. There is a strong correlation indicating that the diffuse radiation field is dependent on nearby stars. By contrast, there is no correlation with the amount of H I in the line of sight (b) and very little with the Galactic latitude (c).

TABLE 4
LIMITS ON THE EXTRAGALACTIC BACKGROUND

<i>l</i> (deg)	<i>b</i> (deg)	Background ^a	1 σ Error ^a	<i>N</i> (H I) ($\times 10^{22}$ cm)	1 σ Upper Limit ^a
70.7	-30.0	0	28	0.071	28
17.7	-52.2	0	33	0.063	33
175.4	-75.7	0	37	0.077	37
17.7	-52.2	0	38	0.063	38
17.7	-52.2	0	42	0.063	42
106.2	83.9	0	49	0.039	49
97.2	71.6	0	50	0.028	50
177.2	-67.3	0	50	0.17	50
331.7	-71.1	0	51	0.030	51
267.6	74.3	0	52	0.11	52
64.4	-69.6	0	54	0.13	54
155.1	75.1	0	60	0.028	60
277.2	-71.5	0	62	0.038	62
91.1	61.4	0	62	0.026	62
280.0	-24.9	0	65	0.034	65
166.6	-79.5	0	70	0.070	70
356.4	-53.2	0	71	0.029	71
115.0	46.9	0	71	0.015	71
105.5	49.1	0	77	0.013	77
99.3	80.3	0	80	0.040	80
32.0	70.5	32	63	0.030	95
54.7	46.1	0	96	0.039	96
201.6	53.9	0	101	0.047	101

^a In photons $\text{cm}^{-2} \text{s}^{-1} \text{sr}^{-1} \text{\AA}^{-1}$.

tabulated in Table 4. Because of the importance of this result, we have plotted the spectrum of one of these points in Figure 10. Our analysis procedure fits a continuum to the entire spectrum between 912 and 1200 \AA ; if, instead, we

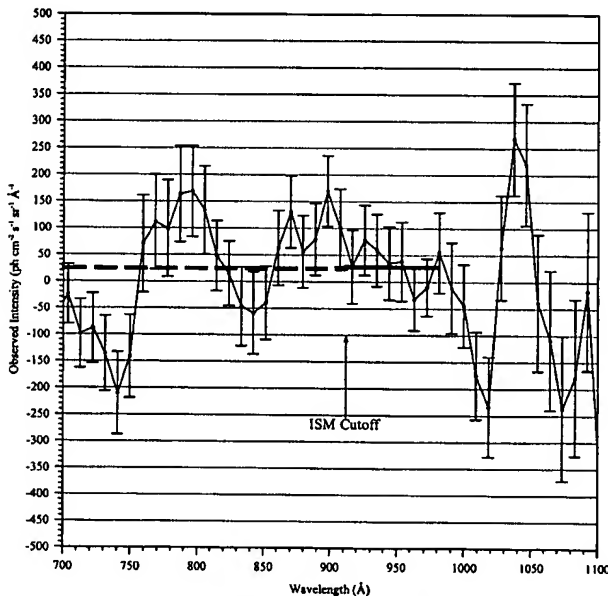


FIG. 10.—Spectrum of one of the best of our extragalactic sight lines (Table 4), plotted here as 1σ error bars. Any astrophysical source would show up as a step in the spectrum at 912 \AA . The two dark lines show the derived background respectively below and above the Lyman limit, using only those points indicated. The difference between the two is only 4 ± 28 photons $\text{cm}^{-2} \text{s}^{-1} \text{sr}^{-1} \text{\AA}^{-1}$, allowing us to set a 1σ limit of less than 30 photons $\text{cm}^{-2} \text{s}^{-1} \text{sr}^{-1} \text{\AA}^{-1}$ on the level of an isotropic extragalactic background. We note that we do not explicitly account for systematic errors, which may be at the same level as the photon noise.

simply take the weighted sum of the points immediately above and below the ISM cutoff, we get the same answer (4 ± 28 photons $\text{cm}^{-2} \text{s}^{-1} \text{sr}^{-1} \text{\AA}^{-1}$). The limits we place on the extragalactic continuum emission are much lower than the canonical value of about 300 photons $\text{cm}^{-2} \text{s}^{-1} \text{sr}^{-1} \text{\AA}^{-1}$ obtained at wavelengths greater than Ly α , and Henry (1991) has suggested that much of the extragalactic emission longward of Ly α is due to recombination radiation from intergalactic Ly α clouds.

5. CONCLUSIONS

We have reduced the entire set of archival *Voyager* data from launch until early 1994, comprising more than 17 years and 8000 observations. Out of these, we have selected 431 as observations of the diffuse radiation field with no point-source contamination. There is a large range in the observed intensity from each of these regions ranging from 1σ upper limits of as low as 30 photons $\text{cm}^{-2} \text{s}^{-1} \text{sr}^{-1} \text{\AA}^{-1}$ to a detection of over 30,000 photons $\text{cm}^{-2} \text{s}^{-1} \text{sr}^{-1} \text{\AA}^{-1}$ near the star λ Lib. The level of the diffuse radiation field is correlated with the presence of nearby bright stars and is due to local effects. Accordingly, there is no correlation with the amount of neutral hydrogen in the line of sight and only a minor correlation with the Galactic latitude. The dark regions allow us to constrain the extragalactic flux on which our best (1σ) limits are 30 photons $\text{cm}^{-2} \text{s}^{-1} \text{sr}^{-1} \text{\AA}^{-1}$. We have not included systematic errors, which are likely to be on the same level, in this analysis.

We have successfully modeled the observed intensity of the resonantly H I Ly α and He I λ 584 heliospheric emission lines in the outer solar system. Using simple analytic expressions that theoretically describe a combination of optically thin and optically thick scattering regimes, a power-law distance dependence, and a time dependence proportion to observed solar Ly α intensities, we have characterized the

observed line intensities over the range of heliospheric distances from 15 to 50 AU.

Our major plans for the future include studying some of the specific *Voyager* observations in more detail, such as that near λ Lib, which appears to be a reflection nebula near the star. We are using these data to refine our model of the dust-scattered starlight to predict the optical constants of the interstellar dust grains in this previously unexplored wavelength region. The *Voyager* archives are likely to be the most comprehensive, and indeed the only source of

information about the UV radiation field in the crucial spectral region between 912 and 1200 Å for quite some time into the future.

This work was supported by NASA grants NAG5-2398 and NAG5-2299 to the Johns Hopkins University. This research has made use of the SIMBAD database, operated as CDS, Strasbourg, France. We thank an anonymous referee for constructive criticism on the first draft of this paper.

REFERENCES

- Belyaev, V. P., Kurt, V. G., Melioranskii, A. S., Smironov, A. S., Sorokin, L. S., & Tilt, V. M. 1971, *Cosmic Res.*, 8, 677
 Bixler, J., Bowyer, S., & Grewing, M. 1984, *A&A*, 141, 422
 Bowyer, S. 1991, *ARA&A*, 29, 59
 Brandt, J. C., & Chamberlain, J. W. 1959, *ApJ*, 130, 670
 Broadfoot, A. L., et al. 1981, *J. Geophys. Res.*, 86, 8259
 Hall, D. T., 1992, Ph.D. thesis, Univ. Arizona
 Hall, D. T., Shemansky, D. E., Judge, D. L., Gangopadhyay, P., & Gruntman, M. A. 1993, *J. Geophys. Res.*, 98, 15185
 Henry, R. C. 1973, *ApJ*, 179, 97
 ———. 1991, *ARA&A*, 29, 89
 Holberg, J. B. 1986, *ApJ*, 311, 969
 ———. 1990, in *IAU Symp. 193, The Galactic and Extragalactic Background Radiation*, ed. S. Bowyer & C. Leinert (Dordrecht: Kluwer), 220
 Holberg, J. B., Ali, B., Carone, T. E., & Polidan, R. S. 1991, *ApJ*, 375, 716
 Holberg, J. B., & Watkins, R. 1992, *Voyager Ultraviolet Spectrometer Guest Observer and Data Analysis Handbook*, Version 1.1, unpublished
 Ivanov, V. V. 1973, *Transfer of Radiation in Spectral Lines*, Vols. 1 and 2 (NBS SP-388; Washington, DC: GPO)
 Lean, J. 1990, *J. Geophys. Res.*, 95, 1433
 Murthy, J., & Henry, R. C. 1995, *ApJ*, 448, 847
 Murthy, J., Henry, R. C., & Holberg, J. B. 1991, *ApJ*, 383, 198
 Pryor, W. R., et al. 1992, *ApJ*, 394, 363
 Quemerais, E., Sandel, B. R., Lallement, R., & Bertaux, J.-L. 1995, *A&A*, 299, 249
 Sandel, B. R., Shemansky, D. E., & Broadfoot, A. L. 1979, *ApJ*, 227, 808
 Sciama, D. W. 1990, *Nature*, 346, 40
 Thomas, G. E. 1978, *Ann. Rev. Earth Planet. Sci.*, 6, 173
 Tobiska, K. 1991, *J. Atmos. Terr. Phys.*, 53, 1005